NANO LETTERS
Cite This: Nano Lett. XXXX, XXX, XXX−XXX
Letter
pubs.acs.org/NanoLett

# Coupling Single Photons from Discrete Quantum Emitters in $WSe_2$ to Lithographically Defined Plasmonic Slot Waveguides

M. Blauth,[†,‡] M. Jürgensen,[†] G. Vest,[†] O. Hartwig,[†] M. Prechtl,[†] J. Cerne,[†,§] J. J. Finley,*[,†,‡] and M. Kaniber*[,†,‡]

[†]Walter Schottky Institut and Physik Department, Technische Universität München, Am Coulombwall 4, 85748 Garching, Germany
[‡]Nanosystems Initiative Munich (NIM), Schellingstr. 4, 80799 Munich, Germany
[§]Department of Physics, University at Buffalo, The State University of New York, Buffalo, New York 14260, United States

Supporting Information

**ABSTRACT:** We report the observation of the generation and routing of single plasmons generated by localized excitons in a $WSe_2$ monolayer flake exfoliated onto lithographically defined Au-plasmonic waveguides. Statistical analysis of the position of different quantum emitters shows that they are $(3.3 \pm 0.7)$ times more likely to form close to the edges of the plasmonic waveguides. By characterizing individual emitters, we confirm their single-photon character via the observation of antibunching in the signal ($g^{(2)}(0) = 0.42$) and demonstrate that specific emitters couple to modes of the proximal plasmonic waveguide. Time-resolved measurements performed on emitters close to and far away from the plasmonic nanostructures indicate that Purcell factors up to $15 \pm 3$ occur, depending on the precise location of the quantum emitter relative to the tightly confined plasmonic mode. Measurement of the point spread function of five quantum emitters relative to the waveguide with <50 nm precision is compared with numerical simulations to demonstrate the potential for greater increases in the coupling efficiency for ideally positioned emitters. The integration of such strain-induced quantum emitters with deterministic plasmonic routing is a step toward deep-subwavelength on-chip single quantum light sources.

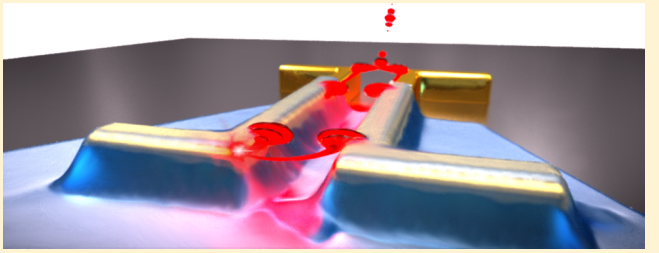

**KEYWORDS:** *Plasmonics, quantum plasmonics, localized excitons, $WSe_2$, slot waveguide*

Downscaling of integrated devices for information technologies is fueled by the need to reduce the energy overhead per bit of data processed.[1−4] It was already recognized several decades ago that shifting from electronic to photonic devices[5,6] promises ultra-high-rate data processing, with maximum accessible clock speeds beyond approximately terahertz.[7] In terms of the energy required to process a single bit of information, all-optical approaches lead the way. Nonlinear interactions can occur in nanophotonic devices and circuits already at the few-photon limit, corresponding to an energy-per-bit budget in the deep sub-femtojoule regime.[8] As such, research into quantum light sources capable of delivering nonclassical states of light (single and few-photon states)[9] into integrated photonic circuits are of strong interest, especially if they are capable of operating at elevated temperature. In these respects, transition-metal dichalcogenides (TMDCs) have captured the attention of many groups worldwide. Monolayers of 2H-stacked TMDCs are direct gap semiconductors[10,11] and have very large exciton binding energies (∼200 to 500 meV) and small excitonic Bohr radii of only a few nanometers.[12,13] Moreover, they can exhibit near-unity internal quantum efficiencies when suitably processed,[14] and the local exciton binding energy is sensitive to the proximal dielectric environment on the nanometer scale[15] and the presence of strain.[16] It has been shown that single photon emitters occur naturally in mechanically exfoliated $WSe_2$[16−20] and that they can be positioned by engineering the local strain field.[21−23] At the same time, the very strong spin−orbit interactions in TMDCs provide unique optical access to spin and valley degrees of freedom,[24−28] providing additional scope for encoding information. Beyond low-energy switching, a clear disadvantage of integrated photonic approaches to information processing is that the lower bound on the size of conventional components is fundamentally limited to the order of the optical wavelength.[29] This results in far lower integration densities as compared to integrated electronics. In this respect, plasmonics offers one way to deliver deep-subwavelength confinement at optical frequencies,[5] and, when combined with novel light-emitting materials, this raises the potential for photonic and quantum devices on the nanoscale. Recent experiments have demonstrated coupling to plasmonic modes in chemically synthesized nanowires for both free exciton[30−32] and localized exciton[33] emission; recent reports obtain coupling to dielectric waveguides.[34]

**Received:** July 2, 2018
**Revised:** August 22, 2018
**Published:** August 28, 2018






DOI: 10.1021/acs.nanolett.8b02687
Nano Lett. XXXX, XXX, XXX−XXX

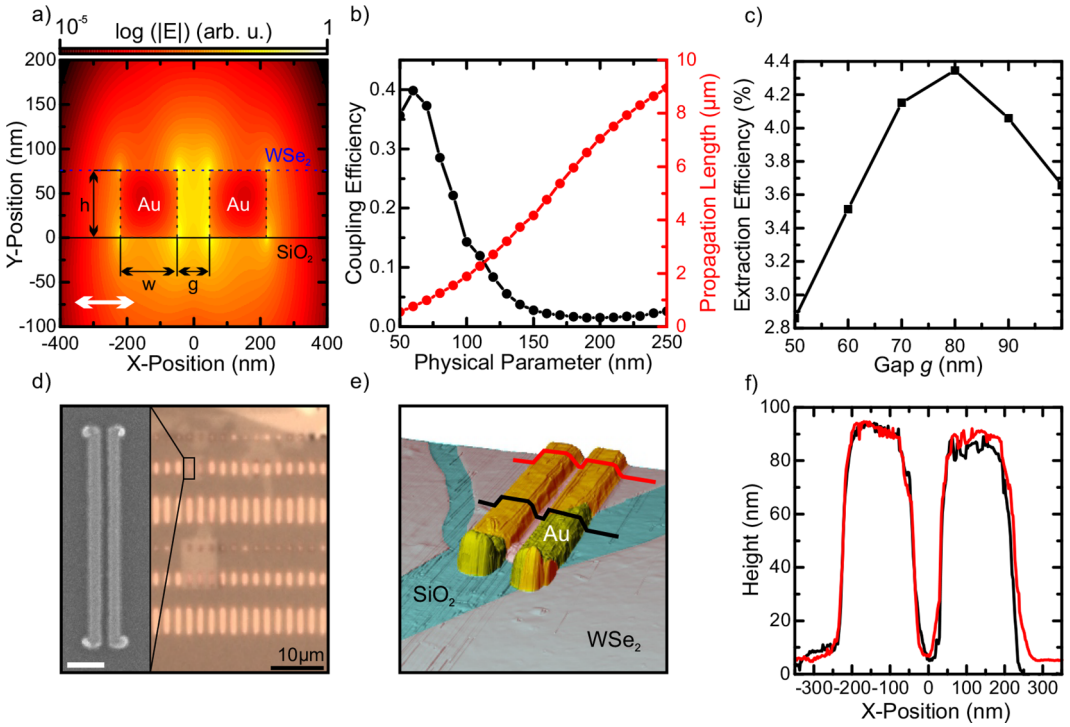


**Figure 1.** Overview of the composite structure. (a) Electric-field distribution of the antisymmetric plasmonic mode supported by the slot-waveguide system calculated using Lumerical MODE Solution.[35] Labels indicate geometric parameters gap, $g$, width, $w$, and height, $h$. White arrow indicates linear polarization orthogonal to the waveguide axis. (b) Geometry-dependent trade-off between induced light−matter interaction and propagation length for $g = w = h$. (c) Combined figure of merit for light extraction from the TMDC monolayer. (d) Optical microscope image of the fabricated plasmonic slot-waveguide array covered by a $WSe_2$ monolayer flake. Inset: SEM image of an individual waveguide including outcoupling structures at both ends; scale bar: 0.5 $\mu$m. (e) False-color, perspective view of an atomic force microscope (AFM) image of the combined system. Labels indicate $SiO_2$ substrate (light blue), $WSe_2$ monolayer (gray), and slot waveguide (yellow), respectively. Curves (black, red) indicate positions of height profiles displayed in panel f. (f) AFM profiles of fully covered waveguide location (red) and partially covered waveguide (black).

Here we mechanically exfoliate a monolayer flake of $WSe_2$ and transfer it onto a lithographically defined plasmonic waveguide. This enables us to probe interactions between localized excitons in the $WSe_2$ flake and tightly confined plasmonic modes. The use of electron-beam lithography provides full control over the position and geometry of the plasmonic waveguide, facilitating deterministic routing of single photons (and plasmons) on-chip. The lithographically defined waveguide creates a nonplanar substrate topography that results in local strain-induced, discrete emitters in the monolayer. The occurrence of such quantum emitters is shown to be 3.3 ± 0.7× more likely in the immediate vicinity (≤0.5 $\mu$m) of the waveguides as compared with unpatterned regions of the sample. The quantum nature of the emitters is confirmed by measuring the second-order intensity correlation function, and spatially resolved measurements demonstrate that single photons are selectively coupled to the plasmonic waveguide mode. Using time-resolved spectroscopy, we show that emitters close to the waveguide (<0.5 $\mu$m) exhibit Purcell factors in the range $F_P \approx 2-15$. By careful determination of the position of five quantum emitters relative to the waveguide with sub-50 nm precision via their point spread function and performing numerical simulations, we demonstrate the potential for significant further increases in coupling efficiency. Our results pave the way toward novel on-chip single plasmon light sources at the nanoscale with the possibility for integration.

The plasmonic slot waveguides investigated here consist of two metal strips separated by a dielectric slot. Figure 1a depicts a cross-sectional sketch for the composite system consisting of a $WSe_2$ monolayer (blue dotted line) covering two metal bars with height, $h$, and width, $w$, separated by a gap, $g$, on top of a $SiO_2$ substrate. The false-color scale displays the electric-field distribution of the antisymmetric fundamental mode for $w$ = 172 nm, $g$ = 96 nm, and $h$ = 75 nm computed using a finite difference eigenmode solver.[35] For this mode, the electric field is maximum at the inner edges of the plasmonic waveguide and the plasmonic field is polarized along the $x$ axis, as indicated by the white arrow. In addition, the waveguide also supports a symmetric mode that is polarized along the propagation direction and exhibits comparable propagation lengths as the fundamental mode. The black curve in Figure 1b shows the simulated coupling efficiency, that is, the probability of an exciton decaying into the plasmonic modes supplied by the waveguide as a function of scaling $g = w = h$. On the basis of the dipole interaction Hamiltonian, the coupling efficiency scales with $|E_{in-plane}|^2$; thus for small feature sizes, strong light−matter interaction is anticipated due to the high local field enhancement. The coupling efficiency decreases with increasing structure size, becoming negligibly small once $g = w = h$ = 150 nm due to weak confinement of the plasmonic mode. Conversely, the propagation length (red curve) increases with increasing physical dimensions of the structure. To obtain maximum count rates from the detection channel in our experiments, we numerically optimized the geometry of our


DOI: 10.1021/acs.nanolett.8b02687
Nano Lett. XXXX, XXX, XXX−XXX

slot-waveguide structures to maximize the optical power arriving at the end of our waveguides. Hereby, we numerically simulated the coupling of a dipole emitter to the propagating plasmonic mode, establishing the trade-off between the propagation losses, which increase with reducing gap size, $g$, and the coupling strength that increases with reducing $g$. Selected results obtained for a $L = 3$ $\mu$m long waveguide are presented in Figure 1c as a function of gap size, $g$, clearly illustrating the trade-off between coupling strength and propagation losses.

Because the extraction efficiency does not vary strongly with the gap width, we conclude that this geometry is robust with respect to fabrication deviations. More detailed information including the calculation of an optimization figure of merit and the scaling of the geometrical parameters can be found in the Supporting Information.

Slot-waveguide arrays are fabricated on a $SiO_2$ substrate using electron beam lithography and gold evaporation. Here we use $g = 96$ nm, $w = 172$ nm, $h = 75$ nm, and lengths of 1, 3, and 6 $\mu$m optimized for extraction efficiency. In a following step, an all-dry transfer of monolayer $WSe_2$[36] is performed to cover large parts of the waveguide array. Figure 1d shows an optical microscope image of an array of plasmonic slot waveguides fully covered by a $WSe_2$ monolayer. The scanning electron microscopy (SEM) image in the inset shows a detailed view of a single slot waveguide including outcoupling structures at both ends optimized for enhanced far-field coupling.

Figure 1e depicts an atomic force microscope (AFM) image of an individual plasmonic waveguide (yellow), partially covered by a $WSe_2$ monolayer (gray). Red and black curves indicate the locations of two height profiles visible in Figure 1f. For the left metal slab, both profiles are in good agreement, whereas the right slab is covered and uncovered for the red and the black profiles, respectively, resulting in a different edge steepness of the rightmost edge. These observations indicate close adhesion of the monolayer to the underlying metal structures and lead to the expectation of increased tensile strain in the flake close to the waveguide edges.

To determine the influence of the plasmonic waveguides on the TMDC monolayer, we confocally recorded PL from a ca. 3000-$\mu m^2$-sized region of the sample at cryogenic temperatures (15 K) using HeNe excitation (1.96 eV) with a 2 $\mu$W excitation power. Figure 2a depicts the spectrally resolved PL intensity averaged over a large region of the sample consisting of both a pristine $WSe_2$ monolayer and the combined system of plasmonic slot waveguides covered by the same $WSe_2$ monolayer. As reported in literature,[37] we observe the neutral ($X^0$), charged ($X^+$), and localized (L) exciton emission peaks. Moreover, a broad low-energy tail below 1.67 eV is visible. Figure 2b presents a selection of individual PL spectra, revealing spatially strongly localized emission with line widths between 2 and 20 meV distributed in energy between 1.5 and 1.67 eV, thereafter referred to as quantum dots (QDs). Such emitters have been found in a variety of different TMDC materials[16−20] exhibiting single photon emission with line widths down to <100 $\mu$eV[38] depending on choice of substrate and the dielectric encapsulation of the atomically thin material. In this work, the $WSe_2$ monolayer is not encapsulated in hBN due to the large size of the flake needed to cover the explored plasmonic structures. This gives rise to significant dynamical broadening and larger line widths of individual quantum emitters, up to a few millielectronvolts.[39] Previous reports have

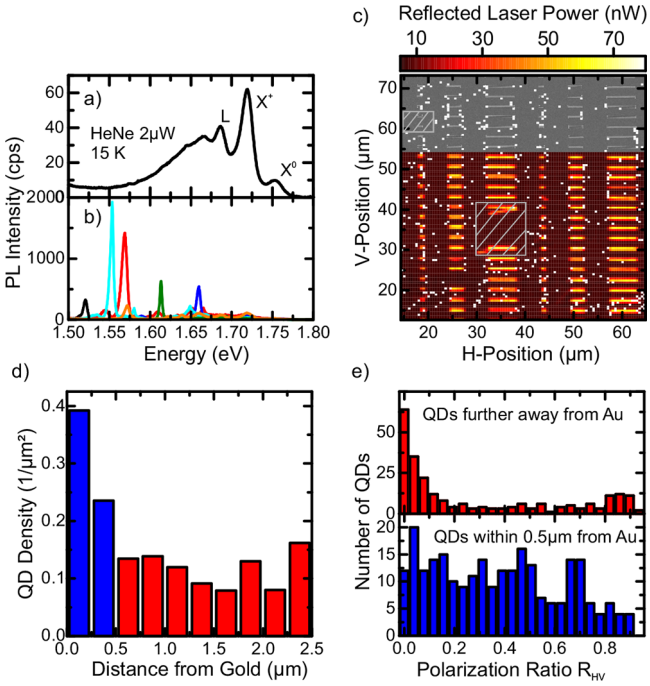


**Figure 2.** Statistical analysis of sharp emission lines occurring at the composite flake-waveguide system. (a) Spatially averaged photoluminescence (PL) spectrum of large $WSe_2$ monolayer region, with labels indicating the respective known spectral features. (b) Selected PL spectra featuring sharp emission lines at different positions strongly deviating from the average spectrum. (c) Large-area confocal PL scan of the sample region exhibiting plasmonic waveguides. Reflected laser power (red color) indicates the positions of the individual waveguides. Superimposed top part shows precise correlation of recorded power data and high-resolution SEM image. White dots indicate locations with isolated sharp emission lines comparable to panel b. Cross-hatched rectangles indicate regions ignored in analysis due to fabrication deviations. (d) QD density as a function of distance of the emitter from the closest waveguide edge exhibiting significantly enhanced QD density for distances <0.5 $\mu$m (blue). (e) Histogram of the number of QDs as a function of degree of polarization measured in $H-V$ basis for QDs closer (further away) than 0.5 $\mu$m in blue (red).

shown that single photon emitters occur at flake edges,[16,17,19] nanobubbles,[40] and positions of high strain[21,41] and allowed positioning via strain engineering.[21] However, the microscopic mechanisms by which excitons are trapped in the experiments presented here are not yet fully clear and remain subject to ongoing investigations. To study the spatial distribution of these QD-like emission lines we simultaneously recorded spatially resolved PL intensity and the reflection of the excitation laser, the latter being displayed in Figure 2c. Because of the enhanced reflectivity of the gold plasmonic waveguides, their position is determined by the reflected excitation laser power. Thus the positions of the individual waveguides could be extracted with high precision, clearly reflecting the arrangement defined during fabrication. To visualize this agreement, the upper part of Figure 2c shows an SEM image of this sample location superimposed onto the reflected laser topography image. All recorded spectra were individually analyzed for sharp emission lines (for details of selection criteria, see the Supporting Information), and positions featuring at least one sharp emission line are marked by a white pixel on Figure 2c. (Cross-hatched rectangles depict regions deviating significantly from the sample design that are


DOI: 10.1021/acs.nanolett.8b02687
Nano Lett. XXXX, XXX, XXX−XXX

ignored to avoid analysis artifacts from fabrication imperfections.) Figure 2d shows a quantitative analysis of the density of sharp emission lines as a function of their respective distance to the closest gold edge. For distances shorter than 0.5 $\mu$m, indicated by blue bars in the Figure, the density of quantum emitters is found to be significantly enhanced compared with larger distances, shown in red. At its highest value of 0.39 $\mu m^{-2}$, the emitter density at the gold edges is enhanced by a factor of (3.3 ± 0.7) with respect to the average density of (0.11 ± 0.03) $\mu m^{-2}$ at distances >0.5 $\mu$m. This enhanced emitter density close to gold structures indicates that the formation probability is closely related to the substrate topography, in good agreement with the findings of previous studies.[21−23] The positions at the waveguide ends exhibit a locally enhanced emitter density that we attribute to the formation of a 2D strain profile, whereas along the waveguide, the strain profile is mainly dominated by 1D strain reducing the probability for full exciton confinement (see the Supporting Information). Therefore, the observed emitter density enhancement presented underestimates the structural influence of the waveguide ends, providing a lower bound for the local QD density.

When performing confocal PL measurements, we simultaneously recorded polarization-resolved spectra with the detection polarization along the waveguide axis ($H$-polarization), and orthogonal to the axis ($V$-polarization). Thus we define a polarization ratio $R_{HV} = |(I_V - I_H)/(I_V + I_H)|$ for each measured discrete emitter in $H-V$ basis. Figure 2d shows a histogram of the distribution of measured polarization ratios. The top panel in red shows the distribution of polarization ratio for emitters located ≥0.5 $\mu$m away from the closest gold edge, corresponding to the data set indicated in red in panel c. The distribution shows a clear maximum around zero and is significantly reduced for higher polarization ratios, indicating that emitters forming far from plasmonic waveguides are predominantly linearly unpolarized. The bottom panel of Figure 2d depicts the polarization ratio distribution for emitters close to the gold structures. Conversely, the distribution of the polarization ratio shows that the number of QDs decreases slowly for increasing polarization ratio, revealing that the polarization is enhanced for emitters close to the plasmonic structures with respect to their unperturbed counterparts. This is consistent with the linear polarization supported by the plasmonic modes, and thus emitters coupling to these modes are expected to reflect this polarization. In addition, both directions H and V coincide with the edges of the plasmonic waveguides, and, as known from literature,[21] the emission polarization is defined by the external strain fields. Both contributions underpin the role of the waveguide in the formation of proximal localized emitters.

We continue to present a thorough characterization of a single typical quantum emitter. Figure 3a depicts a confocally recorded low-temperature PL spectrum at the end of a 3 $\mu$m long plasmonic waveguide excited by 2 $\mu$W of HeNe laser power. The spectrum exhibits a single sharp and spectrally well-isolated emission line and some residual defect PL, indicating the presence of just a single emitter at this position. The inset shows the spectral line shape of this emitter and a Lorentzian fit to the data, from which we extract the time integrated line width to be 2.6 meV. Figure 3b shows polarization-dependent PL intensity and a fit to the data using Malus's law for comparison to the statistical data presented in Figure 2d. We extract the degree of linear

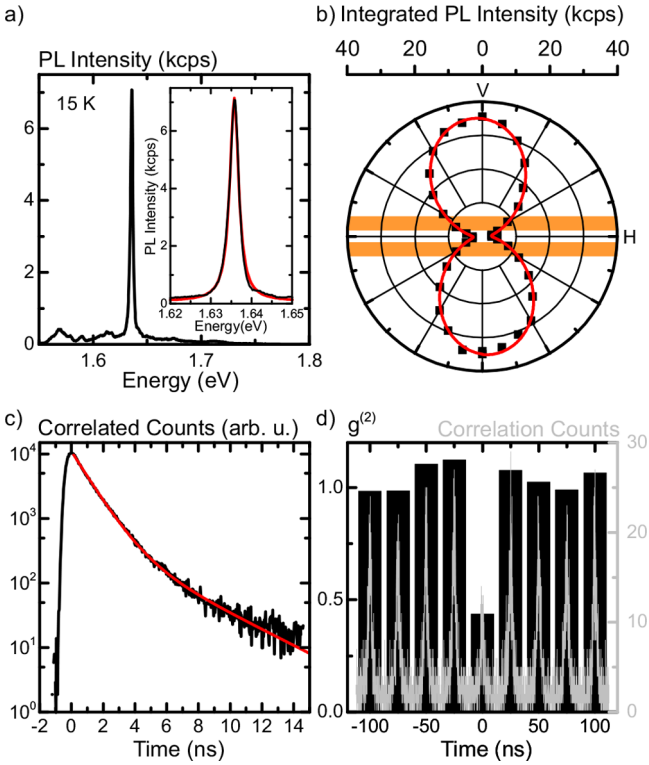


**Figure 3.** Characterization of an individual emitter at the waveguide end. (a) Typical spectrum of a single sharp emission line. Inset: Zoomed spectrum including Lorentzian fit (red) to the raw data (black). (b) Detection polarization measurement of previous emitter (black data points) and $\sin^2$ fit (red) revealing a degree of linear polarization of 85.7% orthogonal to the waveguide axis (orange sketch). (c) Time-resolved PL measurement indicating QD lifetime of (1.07 ± 0.01) ns and corresponding biexponential fit (red). (d) Second-order correlation function obtained from confocal PL measurement in pulsed excitation. Black bars indicate signal binned to the repetition frequency of 40 MHz yielding $g^{(2)}(0) = 0.42$; raw data in gray.

polarization $(I_{max} - I_{min})/(I_{max} + I_{min})$ of 85.7% and clearly observe that the principal polarization axis is oriented along V, that is, perpendicular to the long waveguide axis, as indicated in orange in the same panel. This is consistent with the enhanced polarization ratio discussed in Figure 2e, with the high degree of linear polarization indicating that this particular emitter has formed due to the topography of the underlying waveguide. To perform time-resolved PL measurements, we employed a pulsed laser diode sending 1 $\mu$W CW-equivalent power onto the sample with a pulse duration of ∼90 ps at a repetition rate of 40 MHz. The resulting time-resolved PL intensity is plotted in Figure 3c on a semilogarithmic scale. A biexponential decay fit to the raw data reveals the dominant emitter lifetime of (1.07 ± 0.01) ns and a second weaker contribution with a lifetime of (3.5 ± 0.1) ns. To test the photon statistics, we performed a second-order correlation function measurement using a Hanbury Brown and Twiss setup with confocal detection shown in Figure 3d. As is clearly visible from the data, the peak for zero delay time shows a significantly reduced number of correlations, indicating sub-Poissonian photon statistics consistent with the model that the emission line is due to a single emitter. Significant contribution from dark-signal correlations yield an offset in the raw data that was found to be independent of $\tau$ over the temporal interval


DOI: 10.1021/acs.nanolett.8b02687
Nano Lett. XXXX, XXX, XXX−XXX

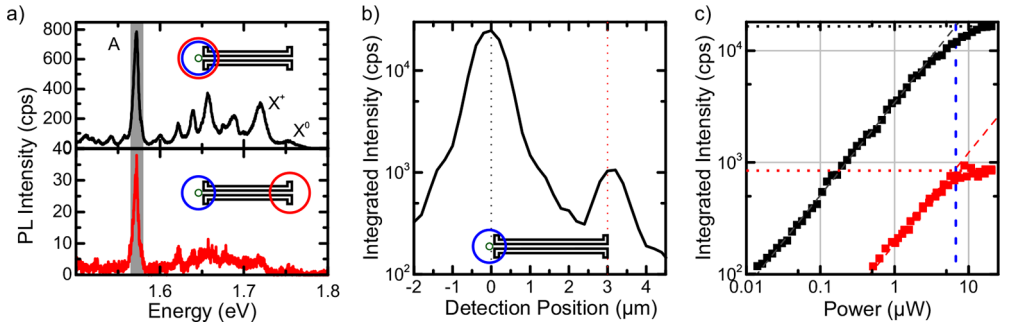


**Figure 4.** Coupling between single emitter and plasmonic slot waveguide. (a) Confocal PL spectrum recorded at the QD position (black curve). Red spectrum recorded with excitation centered on the QD position, with detection located at the remote end of the plasmonic slot waveguide. (b) Detected PL signal integrated over highlighted area in panel a as a function of detection position along the waveguide, with detection position at zero indicating confocal measurement. The initial spatial decay of PL intensity is in agreement with detection spot size; the increase in PL intensity at 3 $\mu$m is consistent with corresponding waveguide length. (c) Power-dependent measurement for confocal and plasmon-mediated configuration in black and red, respectively.

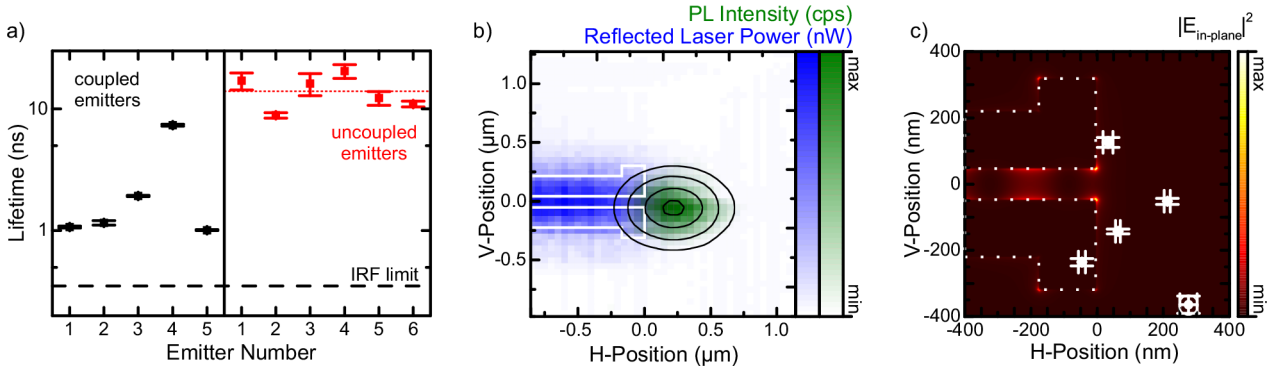


**Figure 5.** Lifetime and location statistics on emitters coupled to plasmonic waveguides. (a) Decay lifetime measurements on coupled (uncoupled) emitters in black (red), with red dotted line indicating the average lifetime of (14 ± 3) ns for uncoupled emitters. Black dashed line indicates IRF time resolution limit. (b) Concurrent high-resolution PL (green) and laser reflectivity (blue) scan revealing the exact relative position of waveguide and QD A, discussed in Figure 4. QD position fitted by 2D Gaussian fit and waveguide outline extracted from reflectivity in black and white, respectively. (c) Simulation of the distribution of $|E_{\text{in-plane}}|^2$ for excited plasmonic waveguide end proportional to the plasmonic coupling efficiency. Location of coupled emitters from panel a indicated in white.

explored in Figure 3d. Thus to enhance the visibility of the $g^2(\tau)$ signal, the individual peaks presented in Figure 3d are binned over each measurement cycle, and the dark-signal contributions are subtracted. The resulting $g^2$ data are presented in Figure 3d as the black histogram. Subsequent comparison of the peak areas results in a $g^{(2)}(0) = 0.42$, proving the single-photon nature of emission from this QD. For second-order correlation measurements on a similar QD yielding $g^2(0) = 0.27$, see the Supporting Information.

We continue to explore the interaction between single emitters and the plasmonic waveguides. The top panel in Figure 4a depicts a low-temperature PL spectrum recorded in confocal geometry, located at the end of a 3 $\mu$m long waveguide. The spectrum shows PL intensity from $X^0$ and $X^+$ as well as several sharp emissions lines visible at lower energy. Here we concentrate on the brightest emission line, labeled A in the Figure, centered at 1.572 eV. By fixing the excitation laser to the emitter position and moving the detection position to the remote end of the waveguide, we recorded the nonconfocal PL intensity depicted in the lower panel in Figure 4a. Here the measured intensity is greatly reduced due to the spatial separation between excitation and detection positions, yet the remaining sharp emission line at 1.572 eV shows an identical spectral footprint to the confocal spectrum. This observation indicates that the QD located at the other end of the waveguide couples directly to the plasmonic mode of the waveguide. To prove this expectation, Figure 4b shows the spectrally integrated PL intensity within the shaded region denoted on panel a as a function of detection position along the waveguide axis with the excitation position fixed to the emitter location. Position zero corresponds to the confocal measurement geometry exhibiting the highest PL intensity. When moving the detection position away from the photo-excited QD, the PL intensity decreases with a spatial Gaussian decay length of (1.52 ± 0.02) $\mu$m, consistent with the detection spot size of 1.58 $\mu$m. However, at a separation of 3 $\mu$m, a significant increase in PL intensity is observed, consistent with scattering of plasmons into the far-field by the out-couplers at the end of the 3 $\mu$m long plasmonic waveguide. Because of the spectrally identical PL signature and the reappearance of the PL signal at the far end of the waveguide, we conclude that the emitter located at one end of the waveguide spontaneously emits into far-field modes as well as into propagating surface plasmon polaritons guided by the plasmonic waveguide. Comparison of emitted luminescence polarization in confocal and plasmon-mediated geometry reveals a comparable degree of linear polarization of both measurements. In addition, the polarization main axis of the emission collected at the remote waveguide end is not always polarized orthogonal to the waveguide. This indicates that the


DOI: 10.1021/acs.nanolett.8b02687
Nano Lett. XXXX, XXX, XXX−XXX

individual emitters couple to both the fundamental and the symmetric plasmonic mode supported by the waveguide. More details of the polarization response can be found in the Supporting Information. To gain insight into the coupling efficiency, Figure 4c shows power-dependent measurements performed at both ends of the waveguide-detected either confocally (black curve) or from the remote end of the plasmonic waveguide (red curve). For low-power HeNe laser excitation, the intensity of both data sets scales with the incident power with an exponent of 0.83 ± 0.01 and 0.81 ± 0.02, respectively, and, for excitation powers higher than 6.7 $\mu$W, both saturate as expected for single photon emitters. This agreement of both quantities strongly indicates that both measurements address the same quantum emitter. In the confocal geometry, the saturation count rate of 1.65 kHz is 19.5× the saturation count rate of 0.85 kHz in the nonconfocal detection.

In principle, the ratio of the saturation intensities for the measurements presented in Figure 4c can be used as a measure of the extraction efficiency of the emitter PL through the waveguide. However, both the far-field radiation pattern and the coupling efficiency to the waveguide are exceptionally sensitive to the precise position of the emitter with respect to the plasmonic waveguide. Therefore, the coupling between the emitters and the corresponding waveguides is assessed via the effective Purcell factor $F_P = \Gamma_{coupled}/\Gamma_{uncoupled}$ by measuring the decay lifetime of the emitters. Because the emitters examined in this manuscript are induced by the underlying topography of the waveguide and thus cannot be investigated emitting purely into vacuum photonic modes, their lifetime is compared to the average lifetime of several ($N$ = 6) reference emitters located far away from a plasmonic waveguide. In Figure 5a, we present the decay times of five (six) coupled (reference) dots plotted with the black (red) data points. The average lifetime of the reference QDs is found to be (14 ± 3) ns. The Purcell factors of the five waveguide coupled emitters shown in Figure 5a, relative to the average decay rate for uncoupled centers, are calculated to vary between 1.9 ± 0.4 and 15 ± 3, where the emitter presented in Figure 4 exhibits a lifetime of (7.4 ± 0.1) ns corresponding to a Purcell factor of $F_P$ = 1.9 ± 0.4. Emitter lifetimes reported in the literature for localized excitons in $WSe_2$ vary strongly from study to study[42] depending on the nature of the emission center and details of the local exciton confinement potential. In our experiments, the saturation count rates of individual emitters were not found to be correlated with the extracted Purcell factors. This observation indicates that inhomogeneities arising from uncontrolled emitter-to-emitter variations of the quantum efficiency between specific radiative centers are significant. The comparison of the saturation count rates of individual quantum emitters with their measured Purcell factor is complicated by the unknown nature of the nonradiative processes in our experiments. Purely radiative rates are influenced by the local density of electromagnetic modes (plasmonic and photonic), whereas nonradiative processes may or may not be linked to the local plasmonic field intensity.

To elucidate the impact of the positioning of emitters relative to the waveguide on the coupling efficiency, we determined the position of the emitter analyzed in Figure 4 with a precision <50 nm by recording its point spread function and that of the waveguide via laser reflectivity. The green color map in Figure 5b shows the result using a step size of only 50 nm. The reflected laser power illustrated by the blue colormap is fitted to extract the position of the waveguide (white outline). The black contour lines indicate the results of a Gaussian fit to the PL intensity data, determining the most likely emitter position relative to the waveguide end ($H$,$V$) = (0,0) to be $\Delta H$ = (210 ± 10) nm and $\Delta V$ = (−50 ± 10) nm. Further details of the fitting procedures are provided in the Supporting Information. Clearly, the emitter is fortuitously positioned relative to the waveguide, such as to allow coupling into the plasmonic mode (Figure 4), but it is also not maximally overlapping with the local plasmonic field, thus accounting for the relatively low measured Purcell factor of 1.9 ± 0.4.

Figure 5c shows the extracted relative positions for the other coupled emitters introduced in panel a, with the error bars indicating the 2$\sigma$ Gaussian fit error of the positions. The waveguide location is indicated by the white dotted line. The false-color data depict the in-plane electric field intensity, expected to be proportional to the emission rate into the plasmonic mode for polarization-averaged emitters. This field distribution varies strongly over length scales of only a few nanometers, and the emitters are distributed around the outcoupling structure. According to the dipole interaction Hamiltonian, the coupling efficiency between the QD and the plasmonic modes is proportional to the scalar product of the local squared electric field and the emission dipole. Therefore, the coupling efficiency strongly varies with both the precise location of the emitter and the orientation of its emission dipole. Consequently, the numerically calculated normalized coupling efficiencies for the marked emitters are distributed between $8 \times 10^{-5}$ and 0.006, taking into account the measured emitter position and dipole orientation for each emitter. In our measurement, this is reflected by a large spread in the lifetime from 1 to 7 ns. Furthermore, it is apparent that none of the measured emitters are located at an absolutely optimum location to produce maximum coupling efficiency. Even the highest of the calculated emission rates is a factor of ∼160 smaller than the corresponding rate for the optimum position and polarization, indicating that the measured Purcell factors of up to 15 ± 3 could still be further increased. The best-case scenario could be approached by more precise strain engineering to ensure that emitters are preferentially created closer to the optimum positions. Furthermore, additional enhancements of the plasmonic coupling could be achieved by improving the emitter quality, for example, by encapsulation in hexagon boron nitride, which has been demonstrated to reduce nonradiative processes for free[39,43,44] and bound excitons.[16]

In summary, we have characterized the emissive properties of an atomically thin layer of $WSe_2$ exfoliated on top of a plasmonic slot waveguide. PL measurements performed at cryogenic temperature revealed the presence of strongly localized excitons with emission line widths between 2 and 20 meV, mostly concentrated around the outcoupling structure of the waveguide. The density of emitters was found to be increased by a factor of at least (3.3 ± 0.7) at positions where the strain field in the flake is high due to the topography of the underlying waveguide structure. Single-photon emission from these emitters was demonstrated by autocorrelation measurements yielding $g^{(2)}(0)$ = 0.42. Finally, the observation of identical spectral features and power dependence of luminescence at both ends of the waveguide confirmed coupling to the plasmonic mode. Thus this hybrid nanophotonic device is capable of generating and routing single photons and plasmons on the nanoscale. Lifetime measure-


DOI: 10.1021/acs.nanolett.8b02687
Nano Lett. XXXX, XXX, XXX−XXX

ments showed Purcell factors between 1.9 ± 0.4 and 15 ± 3 s, and a numerical assessment of the theoretical coupling rates indicates strong potential for further optimization by strain engineering.

## ■ ASSOCIATED CONTENT

### Supporting Information

The Supporting Information is available free of charge on the ACS Publications website at DOI: 10.1021/acs.nanolett.8b02687.

Numerical optimization of slot-waveguide geometry; selection criteria for automated peak analysis; QD PL polarization response to propagation along waveguide; fitting methods for determination of waveguide and emitter positions; statistics on spatial distribution of emitters around waveguides; further second-order correlation measurement (PDF)

## ■ AUTHOR INFORMATION


### Corresponding Authors

*J.J.F.: E-mail: finley@wsi.tum.de.
*M.K.: E-mail: kaniber@wsi.tum.de.

### ORCID

M. Blauth: 0000-0002-3859-4946


### Author Contributions

M.K., J.J.F., and M.B. designed the study. O.H. designed and fabricated the waveguide structures. M.P. exfoliated and transferred monolayers. M.B. built the optical setup and together with M.J. conducted optical measurements and performed the data analysis with support by J.C. and G.V. O.H., M.J., and M.B. implemented FDE and FDTD simulations. All authors discussed the results. M.B. and G.V. wrote the manuscript with contributions from all other authors. J.J.F. and M.K. inspired and supervised the project.

### Notes

The authors declare no competing financial interest.

## ■ ACKNOWLEDGMENTS

We gratefully acknowledge financial support from the DFG via the German Excellence Initiative via NIM as well as support of the Technische Universität München (TUM) - Institute for Advanced Study, funded by the German Excellence Initiative and the TUM International Graduate School of Science and Engineering (IGSSE). J.C. is supported by NSF-DMR1410599 and the Visiting Professor Program from the Bavarian State Ministry for Science, Research & the Arts.

## ■ REFERENCES


(1) Schaller, R. R. *IEEE Spectrum* **1997**, *34*, 52−59.
(2) Ha, D.; Yang, C.; Lee, J.; Lee, S.; Lee, S. H.; Seo, K.-I.; Oh, H. S.; Hwang, E. C.; Do, S. W.; Park, S. C.; et al. *2017 Symposium on VLSI Technology* **2017**, T68−T69.
(3) Wu, S.-Y.; Lin, C.; Chiang, M.; Liaw, J.; Cheng, J.; Yang, S.; Tsai, C.; Chen, P.; Miyashita, T.; Chang, C.; et al. *2016 IEEE International Electron Devices Meeting (IEDM)* **2016**, 2.6.1−2.6.4.
(4) Kish, L. B. *Phys. Lett. A* **2002**, *305*, 144−149.
(5) Ozbay, E. *Science* **2006**, *311*, 189−193.
(6) Sorger, V. J.; Oulton, R. F.; Ma, R.-M.; Zhang, X. *MRS Bull.* **2012**, *37*, 728−738.
(7) Heuring, V. P.; Jordan, H. F.; Pratt, J. P. *Appl. Opt.* **1992**, *31*, 3213.
(8) Nozaki, K.; Tanabe, T.; Shinya, A.; Matsuo, S.; Sato, T.; Taniyama, H.; Notomi, M. *Nat. Photonics* **2010**, *4*, 477−483.
(9) Aharonovich, I.; Englund, D.; Toth, M. *Nat. Photonics* **2016**, *10*, 631−641.
(10) Splendiani, A.; Sun, L.; Zhang, Y.; Li, T.; Kim, J.; Chim, C.-Y.; Galli, G.; Wang, F. *Nano Lett.* **2010**, *10*, 1271−1275.
(11) Mak, K. F.; Lee, C.; Hone, J.; Shan, J.; Heinz, T. F. *Phys. Rev. Lett.* **2010**, *105*, 136805.
(12) Ugeda, M. M.; Bradley, A. J.; Shi, S.-F.; da Jornada, F. H.; Zhang, Y.; Qiu, D. Y.; Ruan, W.; Mo, S.-K.; Hussain, Z.; Shen, Z.-X.; et al. *Nat. Mater.* **2014**, *13*, 1091−1095.
(13) Chernikov, A.; Berkelbach, T. C.; Hill, H. M.; Rigosi, A.; Li, Y.; Aslan, O. B.; Reichman, D. R.; Hybertsen, M. S.; Heinz, T. F. *Phys. Rev. Lett.* **2014**, *113*, 076802.
(14) Amani, M.; Lien, D.-H.; Kiriya, D.; Xiao, J.; Azcatl, A.; Noh, J.; Madhvapathy, S. R.; Addou, R.; KC, S.; Dubey, M.; et al. *Science* **2015**, *350*, 1065−1068.
(15) Rosner, M.; Steinke, C.; Lorke, M.; Gies, C.; Jahnke, F.; Wehling, T. O. *Nano Lett.* **2016**, *16*, 2322−2327.
(16) Tonndorf, P.; Schmidt, R.; Schneider, R.; Kern, J.; Buscema, M.; Steele, G. A.; Castellanos-Gomez, A.; van der Zant, H. S. J.; Michaelis de Vasconcellos, S.; Bratschitsch, R. *Optica* **2015**, *2*, 347.
(17) Chakraborty, C.; Kinnischtzke, L.; Goodfellow, K. M.; Beams, R.; Vamivakas, A. N. *Nat. Nanotechnol.* **2015**, *10*, 507−511.
(18) He, Y.-M.; Clark, G.; Schaibley, J. R.; He, Y.; Chen, M.-C.; Wei, Y.-J.; Ding, X.; Zhang, Q.; Yao, W.; Xu, X.; et al. *Nat. Nanotechnol.* **2015**, *10*, 497−502.
(19) Koperski, M.; Nogajewski, K.; Arora, A.; Cherkez, V.; Mallet, P.; Veuillen, J.-Y.; Marcus, J.; Kossacki, P.; Potemski, M. *Nat. Nanotechnol.* **2015**, *10*, 503−506.
(20) Srivastava, A.; Sidler, M.; Allain, A. V.; Lembke, D. S.; Kis, A.; Imamoglu, A. *Nat. Nanotechnol.* **2015**, *10*, 491−496.
(21) Kern, J.; Niehues, I.; Tonndorf, P.; Schmidt, R.; Wigger, D.; Schneider, R.; Stiehm, T.; Michaelis de Vasconcellos, S.; Reiter, D. E.; Kuhn, T.; et al. *Adv. Mater.* **2016**, *28*, 7101−7105.
(22) Palacios-Berraquero, C.; Kara, D. M.; Montblanch, A. R.-P.; Barbone, M.; Latawiec, P.; Yoon, D.; Ott, A. K.; Loncar, M.; Ferrari, A. C.; Atatüre, M. *Nat. Commun.* **2017**, *8*, 15093.
(23) Branny, A.; Kumar, S.; Proux, R.; Gerardot, B. D. *Nat. Commun.* **2017**, *8*, 15053.
(24) Xiao, Di.; Liu, G.-B.; Feng, W.; Xu, X.; Yao, W. *Phys. Rev. Lett.* **2012**, *108*, 196802.
(25) Cao, T.; Wang, G.; Han, W.; Ye, H.; Zhu, C.; Shi, J.; Niu, Q.; Tan, P.; Wang, E.; Liu, B.; et al. *Nat. Commun.* **2012**, *3*, 172.
(26) Mak, K. F.; He, K.; Shan, J.; Heinz, T. F. *Nat. Nanotechnol.* **2012**, *7*, 494−498.
(27) Zeng, H.; Dai, J.; Yao, W.; Xiao, D.; Cui, X. *Nat. Nanotechnol.* **2012**, *7*, 490−493.
(28) Sallen, G.; Bouet, L.; Marie, X.; Wang, G.; Zhu, C. R.; Han, W. P.; Lu, Y.; Tan, P. H.; Amand, T.; Liu, B. L. *Phys. Rev. B: Condens. Matter Mater. Phys.* **2012**, *86*, 081301.
(29) Born, M.; Wolf, E.; Bhatia, A. B. *Principles of Optics: Electromagnetic Theory of Propagation, Interference and Diffraction of Light*, 7th ed.; Cambridge University Press: Cambridge, U.K., 2016.
(30) Goodfellow, K. M.; Beams, R.; Chakraborty, C.; Novotny, L.; Vamivakas, A. N. *Optica* **2014**, *1*, 149.
(31) Lee, H. S.; Kim, M. S.; Jin, Y.; Han, G. H.; Lee, Y. H.; Kim, J. *Adv. Opt. Mater.* **2015**, *3*, 943−947.
(32) Zhu, Z.; Yuan, J.; Zhou, H.; Hu, J.; Zhang, J.; Wei, C.; Yu, F.; Chen, S.; Lan, Y.; Yang, Y.; et al. *ACS Photonics* **2016**, *3*, 869−874.
(33) Cai, T.; Dutta, S.; Aghaeimeibodi, S.; Yang, Z.; Nah, S.; Fourkas, J. T.; Waks, E. *Nano Lett.* **2017**, *17*, 6564−6568.
(34) Tonndorf, P.; Del Pozo-Zamudio, O.; Gruhler, N.; Kern, J.; Schmidt, R.; Dmitriev, A. I.; Bakhtinov, A. P.; Tartakovskii, A. I.; Pernice, W.; Michaelis de Vasconcellos, S.; et al. *Nano Lett.* **2017**, *17*, 5446−5451.
(35) Lumerical Solutions, Inc. *Lumerical MODE Solutions*. https://www.lumerical.com/tcad-products/mode/.




DOI: 10.1021/acs.nanolett.8b02687
*Nano Lett.* XXXX, XXX, XXX−XXX

(36) Castellanos-Gomez, A.; Buscema, M.; Molenaar, R.; Singh, V.; Janssen, L.; van der Zant, H. S. J.; Steele, G. A. *2D Mater.* **2014**, *1*, 011002.
(37) Jones, A. M.; Yu, H.; Ghimire, N. J.; Wu, S.; Aivazian, G.; Ross, J. S.; Zhao, B.; Yan, J.; Mandrus, D. G.; Xiao, Di; et al. *Nat. Nanotechnol.* **2013**, *8*, 634−638.
(38) He, Y.-M.; Iff, O.; Lundt, N.; Baumann, V.; Davanco, M.; Srinivasan, K.; Höfling, S.; Schneider, C. *Nat. Commun.* **2016**, *7*, 13409.
(39) Wierzbowski, J.; Klein, J.; Sigger, F.; Straubinger, C.; Kremser, M.; Taniguchi, T.; Watanabe, K.; Wurstbauer, U.; Holleitner, A. W.; Kaniber, M.; et al. *Sci. Rep.* **2017**, *7*, 12383.
(40) Shepard, G. D.; Ajayi, O. A.; Li, X.; Zhu, X.; Hone, J.; Strauf, S. *2D Mater.* **2017**, *4*, 021019.
(41) Kumar, S.; Kaczmarczyk, A.; Gerardot, B. D. *Nano Lett.* **2015**, *15*, 7567−7573.
(42) Tripathi, L. N.; Iff, O.; Betzold, S.; Dusanowski, Ł.; Emmerling, M.; Moon, K.; Lee, Y. J.; Kwon, S.-H.; Höfling, S.; Schneider, C. *ACS Photonics* **2018**, *5*, 1919−1926.
(43) Ajayi, O. A.; Ardelean, J. V.; Shepard, G. D.; Wang, J.; Antony, A.; Taniguchi, T.; Watanabe, K.; Heinz, T. F.; Strauf, S.; Zhu, X.; et al. *2D Mater.* **2017**, *4*, 031011.
(44) Cadiz, F.; Courtade, E.; Robert, C.; Wang, G.; Shen, Y.; Cai, H.; Taniguchi, T.; Watanabe, K.; Carrere, H.; Lagarde, D.; et al. *Phys. Rev. X* **2017**, *7*, 021026.
(45) Dutta, S.; Cai, T.; Buyukkaya, M. A.; Barik, S.; Aghaeimeibodi, S.; Waks, E. Coupling Quantum Emitters in $WSe_2$ Monolayers to a Metal−Insulator−Metal Waveguide. 2018, arXiv:1806.08973 [physics.app-ph]. arXiv.org e-Print archive. https://arxiv.org/abs/1806.08973.

## NOTE ADDED IN PROOF

During the preparation of this manuscript, the authors became aware of unpublished similar work by S. Dutta et al.[45] supporting the results of this publication.


DOI: 10.1021/acs.nanolett.8b02687
*Nano Lett.* XXXX, XXX, XXX−XXX